Self-discharge mechanism of high-voltage KVPO4F for K-ion batteries

Romain Wernert, Long H.B. Nguyen, Antonella Iadecola, François Weill, François Fauth, Laure Monconduit, Dany Carlier, Laurence Croguennec

To cite this version:

Romain Wernert, Long H.B. Nguyen, Antonella Iadecola, François Weill, François Fauth, et al.. Self-discharge mechanism of high-voltage KVPO4F for K-ion batteries. ACS Applied Energy Materials, 2022, 5 (12), pp.14913-14921. 10.1021/acsaem.2c02379 . hal-03857373

HAL Id: hal-03857373
https://hal.science/hal-03857373

Self-discharge mechanism of high voltage $KVPO_4F$ for K-ion batteries

Romain Wernert[†‡Δ], Long H.B. Nguyen[†‡Δ], Antonella Iadecola[Δ], François Weill[†Δ||], François Fauth[§], Laure Monconduit[‡Δ||], Dany Carlier[†Δ||*], Laurence Croguennec[†Δ||*]

AUTHOR ADDRESS

† Univ. Bordeaux, CNRS, Bordeaux INP, ICMCB, UMR 5026, F-33600 Pessac, France

‡ ICGM, Université de Montpellier, CNRS, ENSCM, 34095 Montpellier, France

Δ RS2E, Réseau Français sur le Stockage Electrochimique de l'Energie, FR CNRS #3459, Amiens F-80039 Cedex 1, France

§ CELLS-ALBA synchrotron, E-08290, Cerdanyola del Vallès, Barcelona, Spain

|| ALISTORE-ERI European Research Institute, FR CNRS 3104, F-80039 Amiens Cedex 1, France

KEYWORDS: vanadium phosphate fluoride, potassium-ion battery, chemical deintercalation, self-discharge mechanism, side reactions.

ABSTRACT:

Current performances of Li, Na or K-ion batteries are mainly limited by the specific capacity of the positive electrode. Therefore, it is important to reach the highest capacity as possible for a given electrode material. Here we investigate the performance limitation of $KVPO_4F$, a prospective material for K-ion batteries but which can deliver only 80% of its theoretical capacity. We discover that the capacity limitation of $KVPO_4F$ is related to a kinetic competition between K^+ deinsertion and side reactions ascribed to the electrolyte degradation at high potentials. Homeotypic VPO_4F can be obtained from $KVPO_4F$ through a chemical deintercalation process, which disproves a possible structural limitation or instability. The deintercalated compound was characterized by electron and X-ray diffraction, X-ray absorption spectroscopy and nuclear magnetic resonance spectroscopy. Despite the structural stability, a spontaneous reaction occurs between the deintercalated K_xVPO_4F ($x < 0.5$) and the electrolyte (0.8 M KPF_6 in ethylene carbonate : diethylene carbonate), with an electron transfer to vanadium compensated by K^+ intercalation. This reaction leads to self-discharge until the open circuit potential is lower than 4.7 V vs K^+/K, corresponding to the $K_{0.5}VPO_4F$ composition.

INTRODUCTION

Electrochemical energy storage systems are expected to become one of the main technologies for stationary storage of intermittent renewable energies such as photovoltaic and wind turbines. Yet, the markets of Li, Co, and Ni, which are widely used in Li-ion batteries, suffer from instability of their price, as demonstrated by the 500 % increase in the price of Li_2CO_3 over 2021. Such a price volatility is detrimental to the sustainability of the supply chain in the near future.[1,2] Na- and K-ion batteries (KIBs) have been proposed as alternatives since Na/K-containing resources are more abundant and have a wide geographical availability. Potassium-ion batteries are attractive prospective candidates due to the low electrochemical potential of K^+/K redox couple and the small Stokes radius of K^+, providing fast diffusion rate in liquid electrolytes.[3–5] Moreover, potassium-ion batteries can operate with graphite negative electrodes contrary to Na-ion batteries, and do not rely on expensive Co- and Ni-based positive electrodes.[6,7] Prussian blue analogues $K_2(Fe,Mn)Fe(CN)_6$ and vanadium oxyfluoride phosphate $KVPO_4F_{1-y}O_y$ ($0 \leq y \leq 1$) are two of the most promising materials for positive electrode in KIBs, possessing theoretical energy densities of 500 to 600 Wh·kg^{-1}.[8,9] Such values, though inferior to state of the art Li-ion NMC622 (700 Wh·kg^{-1}), are competitive to $LiFePO_4$ (586 Wh·kg^{-1}) for example.[10,11]

Potassium prussian blue analogues have a theoretical capacity of 155 mAh·g^{-1} with an average voltage of 3.6 V vs K^+/K and 3.9 V vs K^+/K for $K_2FeFe(CN)_6$ and $K_2MnFe(CN)_6$, respectively.[8,12–15] Such figures yield a theoretical energy density of 550 to 600 Wh·kg^{-1}. However, owing to the low density of Prussian blue analogues (*c.a.* 2.2 g·cm^{-3}), the volumetric energy density is lower than phosphate compounds. Moreover, several crystalline defects can appear during the synthesis, such as $Fe(CN)_6$ vacancies, interstitial water molecules, K^+ vacancies and oxidation of transition metals, which can considerably lower the capacity.[16]

$KVPO_4F$ crystalizes in the $KTiOPO_4$ type (KTP) structure ($Pna2_1$) which can be described as a framework made of VO_4F_2 chains connected by PO_4 tetrahedra. The F site in $KVPO_4F$ structure can be partially or totally substituted by O to form $KVPO_4F_{1-y}O_y$ ($0 \leq y \leq 1$) where each composition crystallizes in $Pna2_1$ as well and forms an anion disordered solid solution. The KTP structure has been highlighted for the high operating voltage of the $V^{4+/3+}$ (4.3 V vs K^+/K), $Ti^{4+/3+}$ (3.2 V vs K^+/K) and even $\{V^{5+/4+}{=}O\}$ (4.3 V vs K^+/K) redox couples.[17–20] Moreover, the density of $KVPO_4F$ is 3.1 g·cm^{-3} (40% more than Prussian blue analogues) which is highly desirable for improving the volumetric energy density of K-ion batteries. Despite its attractive theoretical capacity of 131 mAh·g^{-1}, full electrochemical depotassiation has never been achieved for $KVPO_4F$.[21,22] A typical charge-discharge galvanostatic curve of $KVPO_4F$ shows that only 0.8 K^+ ion per formula unit can be exchanged during the first charge of the battery (**Figure 1**). As a consequence, the actual energy density at the material scale is limited to 450 Wh·kg^{-1} whereas the utilization of one full K^+ would provide more than 560 Wh·kg^{-1}. However, it is unclear whether the impossibility to reach full deintercalation in $KVPO_4F$ is due to structural constraints or kinetic limitations.

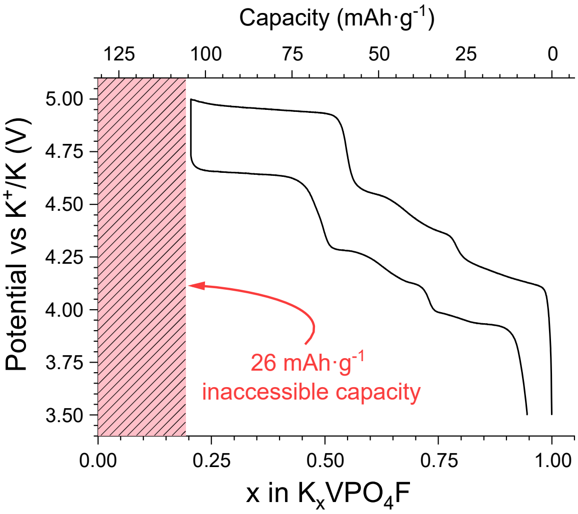

Figure 1: Electrochemical curve of $KVPO_4F$ vs. K metal at C/20. The red hatched area corresponds to the capacity (26 mAh·g^{-1}) that is not accessible in the 3.5 – 5.0 V vs K^+/K voltage window.

Indeed, Caracciolo *et al.* and Kim *et al.* have already demonstrated the effect of side reactions between K_xVPO_4F ($x < 1$) with the 0.8 M KPF_6 in ethylene carbonate : diethylene carbonate electrolyte, leading to a capacity loss upon cycling, especially in the high voltage region (> 4.5 V vs. K^+/K).[21,23] The kinetics of these reactions might prevent K_xVPO_4F from reaching the fully charged state. Indeed, if the alkali deinsertion and parasitic reaction rates are of the same order of magnitude, one can expect a competition between the two phenomena, leading to a lower experimental deinsertion rate than the theoretical one. Such a competition mechanism was proposed by Brutti *et al.* to explain the self-discharge and surface reactivity of $LiCoPO_4$, another high-potential electrode material (4.8 V vs Li^+/Li).[24–26] In this study, several depotassiated K_xVPO_4F samples have been prepared via chemical or electrochemical approach. The structure and electrochemical properties of the depotassiated samples were compared to obtain an insight on the mechanism behind the impossibility of $KVPO_4F_{1-y}O_y$ ($0 \leq y \leq 0.5$) electrode materials to achieve their full theoretical capacity in cycling. Such information is required to establish the interplay between thermodynamic and kinetic factors that control the reactivity of high-voltage electrodes in rechargeable batteries, in such highly reactive K systems.

METHODS AND EXPERIMENTS

Material synthesis. $KVPO_4F$ was obtained by mixing KF (Alfa Aesar) with VPO_4, the latter being synthesized by heating V_2O_5 (99.6%, Sigma-Aldrich) and $NH_4H_2PO_4$ 98% (Sigma-Aldrich) to 850°C for 10 hours under Ar/H_2 atmosphere. The pelletized mixture was then calcined in a argon sealed gold tube at 650°C for 6 hours. The chemical deintercalation of $KVPO_4F$ was conducted under Ar atmosphere according to **Reaction 1**. A solution of 1.3 g (2 equiv.) of NO_2BF_4 (Sigma-Aldrich, > 95 %) dissolved in 200 mL anhydrous acetonitrile (Sigma Aldrich, anhydrous, 99.5 %) was added dropwise into a suspension of 1 g (1 equiv.) of $KVPO_4F$ in 150 mL of acetonitrile . The reaction was carried out for 48 hours at room temperature with a constant magnetic stirring. The product was then rinsed with acetonitrile, vacuum filtered and further dried by evaporating the residual solvent under vacuum.

$$\mathrm{KVPO_4F}\ (s) + \mathrm{NO_2BF_4}\ (sol) \rightarrow \mathrm{K_0VPO_4F}\ (s) + \mathrm{KBF_4}\ (s) + \mathrm{NO_2}(g) \qquad \textbf{Reaction 1}$$

The deintercalated material was then exposed to a solvent mixture or electrolyte by mixing 100 mg of powder in 0.8 mL of ethylene carbonate : diethyl carbonate (EC:DEC 1:1 by vol.%. EC, Sigma-Aldrich, anhydrous, 99%; DEC, Sigma-Aldrich, anhydrous, ⩾99%) without or with 0.8 M KPF_6 (Sigma-Aldrich, ⩾99%), respectively. Such conditions ensure a stoichiometric excess of 2 K^+ ions in the electrolyte per VPO_4F formula unit. The powder was subsequently rinsed with dimethyl carbonate. All the samples were stored in an Ar-filled glovebox. $KVPO_4F_{0.5}O_{0.5}$ was prepared according to our previous work and its chemically deintercalated and electrolyte exposed counterparts were prepared with the same protocol as detailed just above.[20]

Transmission Electron Microscopy (TEM) experiments were performed either with a JEOL 2100 TEM, equipped with a GATAN Orius 200D camera, when Selected Area Electron Diffraction (SAED) was performed, or with a JEOL 2200FS TEM equipped with a Si(Li) JEOL EDX detector for obtaining EDX mapping. Both microscopes operated at 200kV. A suspension of the specimen was prepared in dimethyl carbonate and a drop of the suspension was deposited on a holey carbon coated copper grid. An air-tight sample holder was used to transfer the sample from the glovebox to the TEM.

X-ray diffraction (XRD) experiments were carried out with a laboratory X'Pert3 diffractometer equipped with a capillary spinner and a Cu $K\alpha_{1,2}$ X-ray source. The powder was packed in a 0.5 mm diameter glass capillary and measured with steps of 0.016°. Structural determination of K_0VPO_4F was performed with data measured at ALBA synchrotron (Barcelona, Spain) on BL04-MSPD beamline. The data was collected at $\lambda = 0.61908$ Å, in Debye-Scherrer geometry with the position sensitive MYTHEN detector with a 0.006° effective bin step. The refinement of powder diffraction patterns was carried out with JANA2006 software.[27] The atomic displacement parameters were refined together for all P atoms as well as for all O atoms. A semi-rigid body restraint was applied to the very covalent phosphate groups, allowing the P–O distances to vary between 1.535±0.015 Å.[28] The Bérar-Lelann correction was applied to standard uncertainties.[29] VESTA software was used to visualize the crystal structures.[30]

X-ray absorption spectroscopy (XAS) was performed at synchrotron SOLEIL (Saint-Aubin, France) at ROCK beamline. The samples were measured at V K-edge in transmission geometry with a V foil used as a reference for energy calibration. The oscillating frequency of the Si (111) quick-EXAFS monochromator was set at 2 Hz. The samples were diluted in cellulose to form a 13 mm diameter disk with a mass loading of 4.5 $mg\cdot cm^{-2}$. 600 spectra were averaged for each sample. The energy calibration, spectrum normalization and linear combination fitting were all carried out with DEMETER software.[31]

^{31}P solid-state nuclear magnetic resonance (NMR) spectroscopy was performed with a Bruker Avance III 100 MHz spectrometer, equipped with a 2.4 T wide-bore magnet, leading to a Larmor frequency of 40.6 MHz for ^{31}P. The 2.5 mm rotors were filled with around 15 mg of powder and the magic angle spinning (MAS) frequency was set at 30 kHz. The sequence consisted in a Hahn echo with a 1.7 µs 90° pulse duration and a recycle time of 0.2 s. An aqueous 85 wt. % H_3PO_4 (Sigma-Aldrich) solution was used to reference the chemical shift of ^{31}P at 0 ppm.

Density Functional Theory calculations were performed using the projector-augmented wave (PAW) method with the Vienna *Ab initio* simulation package (VASP) code.[32–37] The generalized gradient approximation (GGA) with Perdew-Burke-Ernzerhof (PBE) exchange-correlation functional was used for all calculations.[38] A Hubbard correction ($U_{eff} = U\text{-}J = 3$ or 5 eV) was used to take into account the self-interaction error of strongly correlated 3d electrons.[39] All calculations were spin-polarized considering a ferromagnetic ordering as required to model NMR Fermi contact shifts.[40] The planewave cutoff energy was set to 600 eV and a 4 × 4 × 4 *k*-mesh was used. The K_0VPO_4F input model was generated by removing all K from the parental $KVPO_4F$ structure. The isotropic hyperfine coupling parameters were computed from the relaxed structure and further used for the calculation of Fermi contact shifts, as described in earlier work of our group.[41–43] Briefly, the theoretical molar magnetic susceptibility of V^{4+} ($\mu_{eff} = 1.76\ \mu_B$) was considered and the Curie-Weiss temperature was hypothesized to be 0 K. The temperature at which the Fermi contact shifts were computed was chosen to be 320 K.

Electrochemical characterisations consisted in cycling self-standing electrodes vs K metal (Alfa Aesar, 99.95%) in CR2032 coin cells. The electrodes were made by mixing active material (impurities included), carbon black (Super P) and PTFE (Sigma Aldrich) in the 80:15:5 ratio (by wt.%). 50 µL of 0.8 M KPF_6 dissolved in a 1:1 volumetric mixture of EC:DEC was used as electrolyte and two polymer fiber mat disks (Viledon, Freudenberg) were used as separators. Electrochemical cycling was performed at C/20 current rate (exchange of 1 K^+ per formula unit in 20 hours) between 3.5 and 5 V vs K^+/K.

RESULTS

Structural characterization. The fully depotassiated, K_0VPO_4F sample, was prepared via a chemical deintercalation with NO_2BF_4 dissolved in acetonitrile media under argon atmosphere. The standard potential of NO_2^+/NO_2 lies at 2.1 V vs NHE, *i.e.* 5.1 V vs K^+/K.[44] The crystal structure of this material was investigated with XRD. The diffractograms of $KVPO_4F$ before and after K desintercalation are compared in **Figure 2a** which shows that the characteristic peaks of $KVPO_4F$ are conserved after chemical deintercalation suggesting that the KTP-type framework is maintained (**Figure 2a**). The Bragg reflections shifted towards higher angles indicating a decrease of the cell parameters upon the K^+ removal process. The splitting of the 201 and 011 peaks highlights a larger decrease of the ***b*** cell parameter compared to ***a***. According to **Reaction 1**, KBF_4 was generated as a by-product during the de-potassiation with NO_2BF_4, which could not be dissolved in any glovebox-compatible solvents (carbonates, acetonitrile…). Besides, TEM-EDX maps (**Figure S1**) clearly show the presence of two different phases, one being V and P rich (spot 1) and the other being K and F rich (spot 2). Thus, KBF_4 stayed as an impurity in all the following investigations.

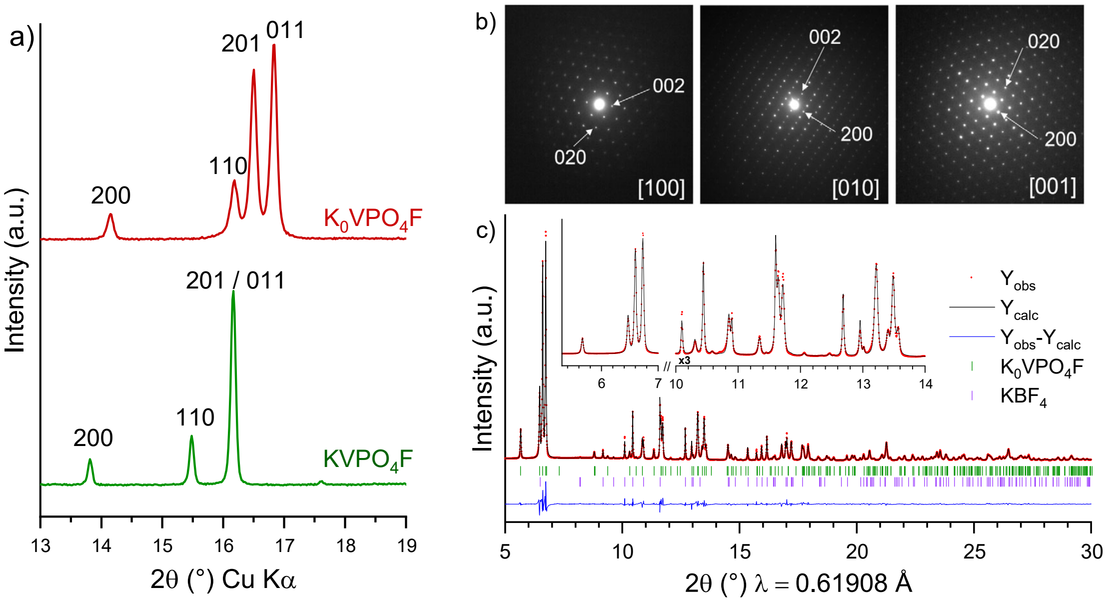

Figure 2: a) X-ray diffraction pattern of the first four Bragg peaks for $KVPO_4F$ and K_0VPO_4F obtained from chemical deintercalation of $KVPO_4F$. b) Representative selected area diffraction patterns of K_0VPO_4F, the three patterns were obtained from the same primary particle. c) Rietveld refinement of the synchrotron XRD pattern collected after the chemical deintercalation of $KVPO_4F$, considering K_0VPO_4F with KBF_4 as by-product.

Fedotov *et al.* have already reported the crystal structure of quasi deintercalated $K_{0.17}VPO_4F$, however its cell parameters are different compared to those of our chemically deintercalated sample.[17] Thus, the crystal structure of highly deintercalated K_xVPO_4F was reinvestigated using selective area electron diffraction combined with synchrotron X-ray diffraction. **Figure 2b** shows the electron diffraction patterns of K_0VPO_4F along the three characteristic zone axes [100], [010] and [001], with the observed reflection conditions $k+l = 2n$, $h = 2n$ and $h+k = 2n$, respectively. It indicates that K_0VPO_4F crystallizes in the *Pnan* space group. Due to the presence of KBF_4 impurity, a two-phases Rietveld refinement was performed on SXRD pattern collected for the chemically deintercalated sample (**Figure 2c**). The refinement shows that K_0VPO_4F has the cell parameters of $a = 12.504(1)$ Å, $b = 6.0875(4)$ Å and $c = 10.462(1)$ Å, corresponding to a 9.2% cell volume decrease compared to $KVPO_4F$. The full K^+ deintercalation is supported by i) no major residual electron density in the structural tunnels is observed on the Fourier difference maps (**Figure S2**), ii) the occupancy of K(1) and K(2) site converging to 0 and iii) the quantification of KBF_4 phase fraction (39 wt. %) very close to the 43 wt.% as expected from **Reaction 1**. The detailed crystallographic description of K_0VPO_4F is given in **Table S1**. From these structural characterisations, it can be concluded that KTP-type framework is stable at the fully de-intercalated state as no significant structural rearrangement occurs even with fully empty alkali sites.

The deintercalated compound K_0VPO_4F was further characterised by X-ray absorption spectroscopy in order to assess the vanadium oxidation state. The X-ray absorption near edge structure (XANES) spectra, featuring the $1s \rightarrow 4p$ dipole allowed transitions, of some selected references, such as $KV^{3+}PO_4F$, $KV^{4+}OPO_4$ and $V^{5+}OPO_4$, are presented together with the spectrum of K_0VPO_4F (**Figure 3a**). For the latter compound, the position of the main edge superposes that of $KVOPO_4$ reference indicating the +4 oxidation state in accordance with a full depotassiation of $KVPO_4F$. The pre-edge region of K_0VPO_4F shows more intense features compared to the pristine compound, indicating a breaking in the centrosymmetry of VO_4F_2 octahedra. Indeed, site distortion evolved from $2.5 \cdot 10^{-4}$ and $3.3 \cdot 10^{-4}$ for $V(1)_{cis}$ and $V(2)_{trans}$ respectively in $KVPO_4F$ to $17.2 \cdot 10^{-4}$ and $4.4 \cdot 10^{-4}$ in K_0VPO_4F (**Table S1**). In $KVOPO_4$, the site distortion is $37.2 \cdot 10^{-4}$ and $68.4 \cdot 10^{-4}$ which is consistent with the even more intense pre-edge, as such distorted octahedral environments induce mixing of V $3d$–$4p$ orbitals and hence allows the $1s \rightarrow 3d$ transitions to occur.

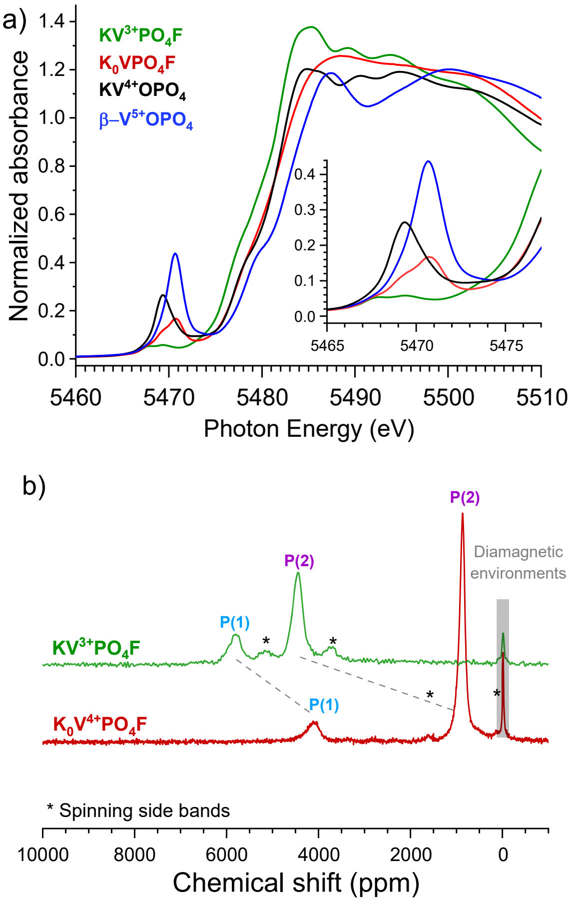

Figure 3: a) V K-edge XANES spectrum of K_0VPO_4F at the V K-edge along with $V^{3+/4+/5+}$ phosphate references. b) ^{31}P MAS-NMR spectra of K_0VPO_4F and $KVPO_4F$ recorded at $B_0 = 2.4$ T. The spinning sidebands are indicated by asterisks.

^{31}P MAS-NMR spectrum of $KVPO_4F$ (**Figure 3b**) shows two intense resonances that were previously attributed to P(1) and P(2) crystallographic sites being surrounded by four V^{3+}.[20] The large ^{31}P NMR shifts (5800 and 4500 ppm) result from the Fermi contact interaction between vanadium's unpaired electrons ($3d^2$ electronic configuration) and phosphorus nuclei. In a similar way, the NMR spectra of K_0VPO_4F displays two main peaks at 4120 ppm and 865 ppm (**Figure 3b**). In K_0VPO_4F, V exhibits the +4 oxidation state with the $3d^1$ electronic configuration and thus the magnitude of the Fermi contact interaction is much weaker and lower ^{31}P NMR shift values are expected as compared to $KVPO_4F$. Nonetheless, the resonance at 4120 ppm indicates that a strong Fermi contact interaction remains between V^{4+} ions and the P1 sites. DFT calculations were carried out to understand the spin transfer mechanism in the K_0VPO_4F structure. The input model for K_0VPO_4F was generated by removing all K from the parental $KVPO_4F$ structure and relaxed using the GGA+U approach with $U_{eff} = 3$ or 5 eV. The cell parameters and bond lengths of the relaxed structure agreed with those observed by TEM and SXRD refinements (**Table S2**). The bond distances range from 1.89 Å to 1.96 Å for V-O and 1.94 Å to 2.02 Å for V-F indicating as expected more ionic bonding towards fluorine than oxygen.

Spin density maps around the P(1) and P(2) crystallographic sites (**Figure 4**) show the spatial distribution of "spin up" electrons. For both vanadium sites, a single t_{2g} orbital is occupied, indicating a lift of (d_{xy}, d_{yz}, d_{xz}) degeneracy. All the orbitals containing vanadium's electron spin pointed their lobes towards P(1) site (**Figure 4** and **Figure S3**) for a proper $d(V^{IV})–p_{\pi}(O)–sp^3(P)$ interaction[20], the P(1) site thus receives the electron spin from the four surrounding vanadium atoms with a strong Fermi contact. On the contrary, around P(2) each of the spin containing orbital plane of V^{4+} are quasi perpendicular to the V–O–P bond path, thus geometrically limiting the strength of the interaction (**Figure 4**) due to the absence of V–O π overlap. This is further supported by the presence of spin density around P(1) (**Figure S3**), forming two crescents, whereas no spin density is observed around P(2) at 10^{-3} spin·Å^{-3}. Finally, The theoretical Fermi contact shifts of P(1) and P(2) in K_0VPO_4F calculated using GGA+U method are given in **Table 1**. Whatever the U_{eff} value is, the predicted shift for P(1) is approximately five times higher than for P(2), which is consistent with experimental observations.

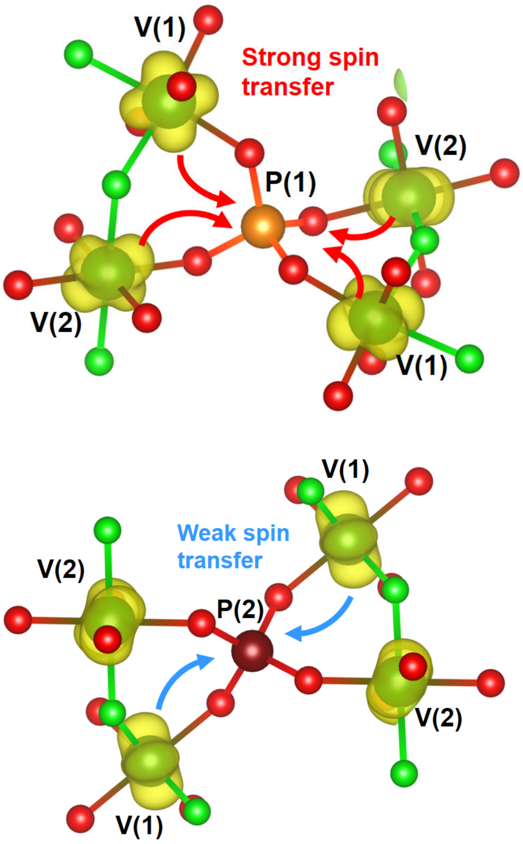

Figure 4: Spin density maps of the P(1) and P(2) local environments showing the majority spin in yellow with isosurface of $5 \cdot 10^{-3}$ spin·Å^{-3} for the calculation performed with $U_{eff} = 5$ eV. Only the "spin-up" density is shown for clarity.

K_0VPO_4F stability in electrochemical reactions. The results obtained so far have shown that K_0VPO_4F can be chemically isolated as a stable phase; nonetheless, full capacity could not be achieved from $KVPO_4F$ during electrochemical reactions. The chemical stability of K_0VPO_4F was thus explored by exposing the powder to either the EC:DEC mixture solvent (1:1 by volume) or the electrolyte, consisting in 0.8 M KPF_6 dissolved in the previous solvent mixture. The unchanged diffractograms before and after exposure to the solvent demonstrate that this treatment does not affect the crystal structure (**Figure S4**). However, a radical change of the long-range structure was detected when the deintercalated compound was exposed to the electrolyte.

Table 1: Experimental and computed ^{31}P NMR shifts for K_0VPO_4F

	Experimental shift (ppm)	GGA + 3 eV (ppm)	GGA + 5 eV (ppm)
P(1)	4120	6169	5271
P(2)	865	1360	986

Table 2: Cell parameters retrieved by XRD refinement for $KVPO_4F$, K_0VPO_4F and K_xVPO_4F.

	a (Å)	b (Å)	c (Å)	V/Z (Å^3)
$KVPO_4F$	12.8223(1)	6.39721(3)	10.6203(1)	108.90
K_0VPO_4F	12.504(1)	6.0875(5)	10.462(1)	99.54
K_xVPO_4F	12.632(3)	6.142(1)	10.545(3)	102.28

The comparison of XRD patterns in **Figure 5a** shows that after an immersion in the electrolyte, the diffraction peaks became broader and shifted to intermediate positions located between those of $KVPO_4F$ and K_0VPO_4F. The obtained XRD pattern was refined using the *Pnan* space group (**Figure S5**) and cell parameters of the phase were compared to those of $KVPO_4F$ and K_0VPO_4F (**Table 2**). A clear expansion of 2.7 % of the unit cell volume is observed after the electrolyte exposure, which could be due to a spontaneous K^+ insertion in the empty framework. Consequently, this sample will be referred to "K_xVPO_4F" in the rest of the text. The reduction of vanadium should occur concomitantly to compensate the charge, which was fully supported by V K-edge XAS (**Figure 5b**). The edge position of K_xVPO_4F is located between those of $KVPO_4F$ and K_0VPO_4F. Linear combination fitting performed between 5474 and 5510 eV (**Figure S6**), using $KVPO_4F$ and K_0VPO_4F as standards. It suggested that the recovered sample has a $V^{3.5+}$ average oxidation state. Given that the crystal framework is maintained and half of V ions were reduced to V^{3+}, one can expect that the composition of "K_xVPO_4F" is actually $K_{0.5}VPO_4F$. Unfortunately, the direct chemical titration of K^+ content was not possible since the chemically deintercalated powder contained KBF_4 as impurities.

The electrochemical properties of the chemically depotassiated powder, "K_0VPO_4F", were evaluated in a coin cell with metallic K as a negative electrode. The starting point of the electrochemical curve (**Figure 6a**) was set at 0.5 K^+ per VPO_4F unit, consistently with the oxidation state determined from XAS measurements and with the open circuit voltage of the cell measured at 4.7 V vs K^+/K as depicted in **Figure 1**. Moreover, the discharge curve suggests a fully potassiated compound after only 0.5 K^+ inserted into the structure, suggesting that K_0VPO_4F was immediately converted to $K_{0.5}VPO_4F$ when it was in contact with the electrolyte. In the next cycle, the shape of the electrochemical curve in the low potential region (< 4.6 V) was similar to the one of pristine $KVPO_4F$ reported in **Figure 1**, thus indicating that a full potassiation could be achieved starting from K_0VPO_4F. Further charge above 4.5 V was strongly affected by side reactions, leading to a very low coulombic efficiency. Nevertheless, the derivative curve of second discharge (**Figure S7**) overlaps the first one. Overall, the electrochemical tests indicated that the total insertion of 1 mol of K^+ in K_0VPO_4F is possible and reversible.

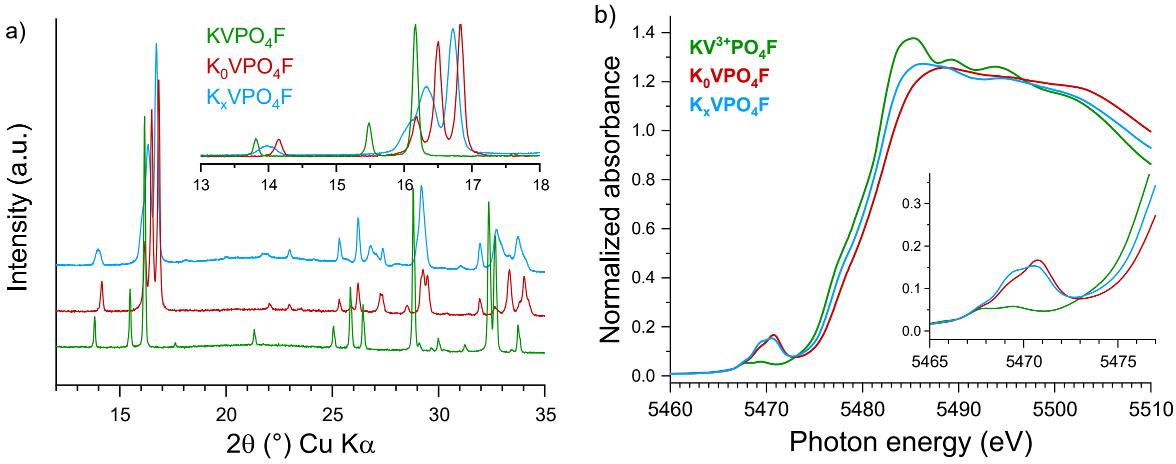

Figure 5: a) X-ray diffraction patterns and b) V K-edge XANES spectra of pristine $KVPO_4F$, chemically deintercalated K_0VPO_4F and electrolyte exposed K_xVPO_4F.

Self-discharge

Hence it seems that the limited capacity originates from an internal mechanism that can be attributed to self-discharge. In order to confirm this hypothesis, a $KVPO_4F||K$ coin cell was assembled and charged up to 5 V vs. K^+/K, resulting in ≈100 mAh·g^{-1} reversible capacity. After the second charge to 5 V, the battery was kept in open-circuit conditions at room temperature for 10 days. The open circuit voltage was recorded (**Figure S8**) and the rest potential decreased gradually from 5 V to 4.75 V during the rest period. Only 65 mAh·g^{-1} (*i.e.* 0.5 K^+ exchanged) was observed in the consequent discharge (**Figure 6b**). The capacity at the high-voltage plateau completely disappeared after the resting period, indicating that the material suffered from a self-discharge at high depotassiated states. Nevertheless, the voltage curve at low potential region (< 4.5 V) was clearly reversible, implying that $K_{0.5}VPO_4F$ was the thermodynamic limit of $KVPO_4F$ system in the current electrolyte.

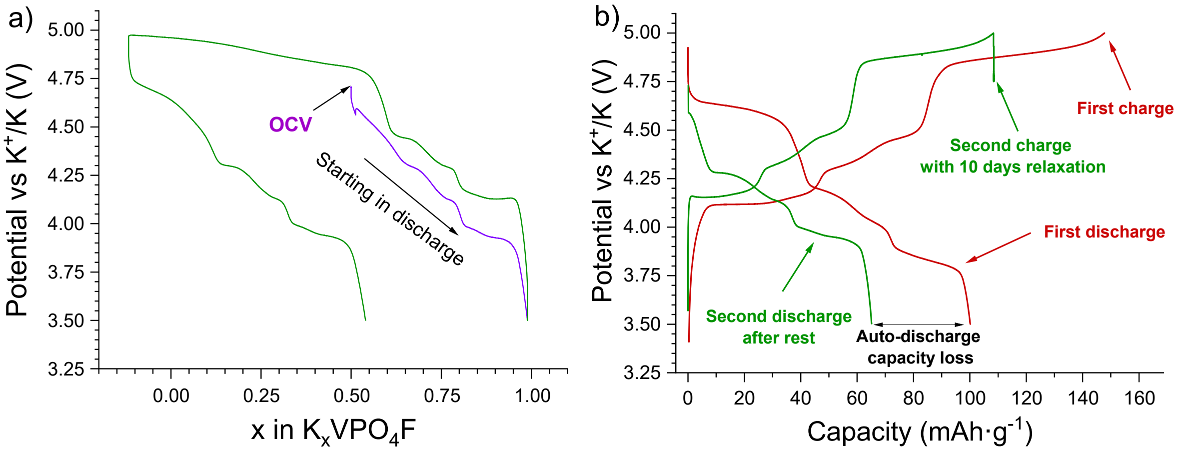

Figure 6: a) Galvanostatic curve obtained for K_0VPO_4F versus K metal at C/20. The initial K^+-content was set at 0.5 corresponding to composition formed when K_0VPO_4F was in direct contact with the electrolyte. b) Comparison of discharge curves obtained for $KVPO_4F$ versus K metal after a first charge without relaxation and a second charge with 10 days relaxation.

GENERAL DISCUSSION

The results previously discussed evidenced, firstly, that K_0VPO_4F composition can be reached and that the structure is stable, secondly, that when exposed to the electrolyte, the compound undergoes spontaneous K uptake and V reduction. Based on these results, we propose the following reaction mechanism: the highly oxidizing power of the material in its highly deintercalated state leads to the decomposition of the electrolyte and involves an electron transfer from decomposing molecules to the vanadium phosphate fluoride. Some V ions are then reduced to V^{3+} and a K^+ ion is spontaneously inserted from the electrolyte to the crystal framework in order to ensure the charge neutrality. Such a mechanism was also proposed by Manzi *et al.* in their earlier work on $LiCoPO_4$.[24,25] The self-discharge mechanism is thermodynamically driven as soon as the electrochemical potential of the active material is higher than that of the electrolyte stability. It involves that this process does not occur only at rest, after a full charge, but that it is a dynamical process which starts during the charge and competes with the K^+ extraction. Indeed, the galvanostatic current applied to charge the battery is a driving force for ion deintercalation whereas the oxidation of the electrolyte reduces the active material and is therefore a competitive driving force for ion re-intercalation. At the end of charge, the two phenomena have similar kinetics that limit the reversible capacity of $KVPO_4F$ at about 80% of the theoretical one.

The same experiments were conducted on the closely related $KVPO_4F_{0.5}O_{0.5}$ compound. Its chemically deintercalated counterpart gives a very similar XRD pattern to that observed for K_0VPO_4F (**Figures S9 and S10**). It can be refined with close cell parameters: $a = 12.481(1)$ Å, $b = 6.092(1)$ Å and $c = 10.546(1)$ Å (**Figures S9 and S10**). The V K-edge XANES spectrum of $K_0VPO_4F_{0.5}O_{0.5}$ lies between those of $KV^{4+}OPO_4$ and $V^{5+}OPO_4$ (**Figure 7a**), which was in line with the expected oxidation state of $V^{4.5+}$. After being exposed to the K^+-containing electrolyte, the edge shifted to lower energy and superposed to that of V^{4+} reference. This observation suggests that $K_0VPO_4F_{0.5}O_{0.5}$ was reduced together with a K^+ insertion for charge compensation. A similar behaviour to that discussed just before for $KVPO_4F$ was thus expected when testing the material in an electrochemical cell. Similarly, we hypothesized the composition $K_{0.5}VPO_4F_{0.5}O_{0.5}$ and started the electrochemical cell in discharge (**Figure 7b**). Here again, the discharge was completed after the reinsertion of 0.5 K^+ and the consecutive charge gives the expected voltage-composition curve for $KVPO_4F_{0.5}O_{0.5}$ versus K metal.

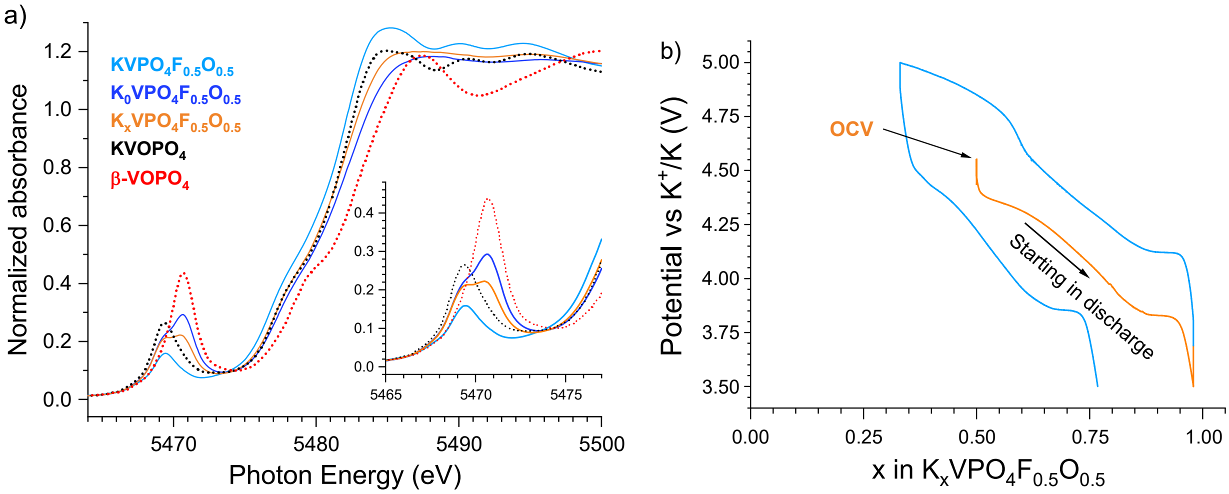

Figure 7: a) XANES spectra at the V K-edge of $KVPO_4F_{0.5}O_{0.5}$ together with its chemically deintercalated and then electrolyte exposed counterparts. $KVOPO_4$ and β-$VOPO_4$ are used as V^{4+} and V^{5+} references, respectively. b) Electrochemical curve of first discharge and successive cycle for $K_0VPO_4F_{0.5}O_{0.5}$ assembled in a half-cell vs K metal.

CONCLUSION

In this work, we demonstrated that the impossibility to electrochemically deintercalate more than 0.8 K^+ ions from $KVPO_4F$ positive electrode was due to a competition between two opposite phenomena. On one hand, the galvanostatic charge drives K^+ deintercalation with simultaneous oxidation of V whereas, on the other hand, the instability of the electrolyte at high potential results in redox degradation reactions, leading to reduction of V concomitantly with insertion of K^+ into the structure. As a consequence, the practical capacity of $KVPO_4F$ is limited to 65 mAh·g^{-1}, that is to say half the theoretical capacity. The study is extended to the $KVPO_4F_{0.5}O_{0.5}$ composition and the same conclusions were drawn. Moreover, this study leads to the discovery, for the first time to our knowledge, of a fully deintercalated KTP-type phosphate with empty tunnels, whose structure was characterized by SXRD, electron diffraction, ^{31}P solid-state NMR coupled with DFT calculations. Finally, our study highlights the interest of combining chemical and electrochemical K insertion/de-insertion to investigate the structure, stability and reactivity of electrode materials.

AUTHOR INFORMATION

Corresponding authors

Laurence Croguennec – Univ. Bordeaux, CNRS, Bordeaux INP, ICMCB, UMR 5026, F-33600 Pessac, France; RS2E, Réseau sur le Stockage Electrochimique de l'Energie, FR CNRS 3459, Amiens F-80039 Cedex 1, France; ALISTORE-ERI European Research Institute, FR CNRS 3104, F-80039 Amiens Cedex 1, France; orcid.org/0000-0002-3018-0992; Email: Laurence.Croguennec@icmcb.cnrs.fr

Dany Carlier – Univ. Bordeaux, CNRS, Bordeaux INP, ICMCB, UMR 5026, F-33600 Pessac, France; RS2E, Réseau sur le Stockage Electrochimique de l'Energie, FR CNRS 3459, Amiens F-80039 Cedex 1, France; ALISTORE-ERI European Research Institute, FR CNRS 3104, F-80039 Amiens Cedex 1, France; orcid.org/0000-0002-5086-4363

Authors

Romain Wernert – Univ. Bordeaux, CNRS, Bordeaux INP, ICMCB, UMR 5026, F-33600 Pessac, France; ICGM, Univ. Montpellier, CNRS, ENSCM, Montpellier, France; RS2E, Réseau sur le Stockage Electrochimique de l'Energie, FR CNRS 3459, Amiens F-80039 Cedex 1, France; orcid.org/0000-0002-5073-4008

Long H. B. Nguyen – Univ. Bordeaux, CNRS, Bordeaux INP, ICMCB, UMR 5026, F-33600 Pessac, France; RS2E, Réseau sur le Stockage Electrochimique de l'Energie, FR CNRS 3459, Amiens F-80039 Cedex 1, France; orcid.org/0000-0001-7823-1595

Antonella Iadecola – RS2E, Réseau sur le Stockage Electrochimique de l'Energie, FR CNRS 3459, Amiens F-80039 Cedex 1, France; orcid.org/0000-0002-9031-8455

François Weill – Univ. Bordeaux, CNRS, Bordeaux INP, ICMCB, UMR 5026, F-33600 Pessac, France; RS2E, Réseau sur le Stockage Electrochimique de l'Energie, FR CNRS 3459, Amiens F-80039 Cedex 1, France; ALISTORE-ERI European Research Institute, FR CNRS 3104, F-80039 Amiens Cedex 1, France;

François Fauth – CELLS-ALBA synchrotron, E-08290, Cerdanyola del Vallès, Barcelona, Spain; orcid.org/0000-0001-9465-3106

Laure Monconduit –ICGM, Univ. Montpellier, CNRS, ENSCM, Montpellier, France; RS2E, Réseau sur le Stockage Electrochimique de l'Energie, FR CNRS 3459, Amiens F-80039 Cedex 1, France; ALISTORE-ERI European Research Institute, FR CNRS 3104, F-80039 Amiens Cedex 1, France; orcid.org/0000-0003-3698-856X

SUPPORTING INFORMATION

Supporting information includes EDX maps, detailed crystal structure solving and crystallographic data, complementary spin density maps and spin transfer mechanism drawings, XANES linear combination fitting, complementary electrochemical characterisations, full pattern matching refinements of K_xVPO_4F and $K_0VPO_4F_{0.5}O_{0.5}$.

ACKNOWLEDGEMENTS

This work was part of the TROPIC project supported by Agence Nationale de la Recherche (ANR) under the grant ANR-19-CE05-0026. ANR is also acknowledged for funding the RS2E network through the STORE-EX Labex Project ANR-10-LABX-76-01. Synchrotron Soleil (France) is acknowledged for providing in house beamtime at the beamline ROCK which also benefits from ANR grant as part of the "Investissements d'Avenir" program ANR-10-EQPX-45. The Mésocentre de Calcul Intensif Aquitain (MCIA) and the modeling center of ISM are acknowledged for computing facilities. We thank Marion Gayot (PLACAMAT UMS CNRS 3626) for operating the TEM-EDX measurements, Cathy Denage, Jérôme Kalisky and Emmanuel Petit (ICMCB) for their technical support.

REFERENCES

(1) Kushnir, D.; Sandén, B. A. The Time Dimension and Lithium Resource Constraints for Electric Vehicles. *Resources Policy* **2012**, *37* (1), 93–103. https://doi.org/10.1016/j.resourpol.2011.11.003.

(2) Olivetti, E. A.; Ceder, G.; Gaustad, G. G.; Fu, X. Lithium-Ion Battery Supply Chain Considerations: Analysis of Potential Bottlenecks in Critical Metals. *Joule* **2017**, *1* (2), 229–243. https://doi.org/10.1016/j.joule.2017.08.019.

(3) Marcus, Y. ANALYTICAL CHEMISTRY DIVISION COMMISSION ON ELECTROANALYTICAL CHEMISTRY. In *Classification and Nomenclature of Electroanalytical Techniques*; Elsevier, 1976; pp 83–95. https://doi.org/10.1016/B978-0-08-021226-5.50002-2.

(4) Matsuda, Y.; Nakashima, H.; Morita, M.; Takasu, Y. Behavior of Some Ions in Mixed Organic Electrolytes of High Energy Density Batteries. *J. Electrochem. Soc.* **1981**, *128* (12), 2552–2556. https://doi.org/10.1149/1.2127289.

(5) Nightingale, E. R. Phenomenological Theory of Ion Solvation. Effective Radii of Hydrated Ions. *J. Phys. Chem.* **1959**, *63* (9), 1381–1387. https://doi.org/10.1021/j150579a011.

(6) Kubota, K.; Dahbi, M.; Hosaka, T.; Kumakura, S.; Komaba, S. Towards K-Ion and Na-Ion Batteries as "Beyond Li-Ion." *Chem. Rec.* **2018**, *18* (4), 459–479. https://doi.org/10.1002/tcr.201700057.

(7) Kim, H.; Kim, J. C.; Bianchini, M.; Seo, D.; Rodriguez-Garcia, J.; Ceder, G. Recent Progress and Perspective in Electrode Materials for K-Ion Batteries. *Adv. Energy Mater.* **2018**, *8* (9), 1702384. https://doi.org/10.1002/aenm.201702384.

(8) Hosaka, T.; Kubota, K.; Hameed, A. S.; Komaba, S. Research Development on K-Ion Batteries. *Chem. Rev.* **2020**, acs.chemrev.9b00463. https://doi.org/10.1021/acs.chemrev.9b00463.

(9) Hosaka, T.; Shimamura, T.; Kubota, K.; Komaba, S. Polyanionic Compounds for Potassium-Ion Batteries. *Chem. Rec.* **2019**, *19* (4), 735–745. https://doi.org/10.1002/tcr.201800143.

(10) Masquelier, C.; Croguennec, L. Polyanionic (Phosphates, Silicates, Sulfates) Frameworks as Electrode Materials for Rechargeable Li (or Na) Batteries. *Chem. Rev.* **2013**, *113* (8), 6552–6591. https://doi.org/10.1021/cr3001862.

(11) Huang, H. Approaching Theoretical Capacity of LiFePO4 at Room Temperature at High Rates. 3.

(12) Zhou, A.; Cheng, W.; Wang, W.; Zhao, Q.; Xie, J.; Zhang, W.; Gao, H.; Xue, L.; Li, J. Hexacyanoferrate-Type Prussian Blue Analogs: Principles and Advances Toward High-Performance Sodium and Potassium Ion Batteries. *Adv. Energy Mater.* **2021**, *11* (2), 2000943. https://doi.org/10.1002/aenm.202000943.

(13) Jiang, X.; Zhang, T.; Yang, L.; Li, G.; Lee, J. Y. A Fe/Mn-Based Prussian Blue Analogue as a K-Rich Cathode Material for Potassium-Ion Batteries. *ChemElectroChem* **2017**, *4* (9), 2237–2242. https://doi.org/10.1002/celc.201700410.

(14) Deng, L.; Qu, J.; Niu, X.; Liu, J.; Zhang, J.; Hong, Y.; Feng, M.; Wang, J.; Hu, M.; Zeng, L.; Zhang, Q.; Guo, L.; Zhu, Y. Defect-Free Potassium Manganese Hexacyanoferrate Cathode Material for High-Performance Potassium-Ion Batteries. *Nat Commun* **2021**, *12* (1), 2167. https://doi.org/10.1038/s41467-021-22499-0.

(15) Wang, B.; Han, Y.; Wang, X.; Bahlawane, N.; Pan, H.; Yan, M.; Jiang, Y. Prussian Blue Analogs for Rechargeable Batteries. *iScience* **2018**, *3*, 110–133. https://doi.org/10.1016/j.isci.2018.04.008.

(16) Hurlbutt, K.; Wheeler, S.; Capone, I.; Pasta, M. Prussian Blue Analogs as Battery Materials. *Joule* **2018**, *2* (10), 1950–1960. https://doi.org/10.1016/j.joule.2018.07.017.

(17) Fedotov, S. S.; Khasanova, N. R.; Samarin, A. Sh.; Drozhzhin, O. A.; Batuk, D.; Karakulina, O. M.; Hadermann, J.; Abakumov, A. M.; Antipov, E. V. AVPO$_4$F (A = Li, K): A 4 V Cathode Material for High-Power Rechargeable Batteries. *Chem. Mater.* **2016**, *28* (2), 411–415. https://doi.org/10.1021/acs.chemmater.5b04065.

(18) Fedotov, S. S.; Luchinin, N. D.; Aksyonov, D. A.; Morozov, A. V.; Ryazantsev, S. V.; Gaboardi, M.; Plaisier, J. R.; Stevenson, K. J.; Abakumov, A. M.; Antipov, E. V. Titanium-Based Potassium-Ion Battery Positive Electrode with Extraordinarily High Redox Potential. *Nat Commun* **2020**, *11* (1), 1484. https://doi.org/10.1038/s41467-020-15244-6.

(19) Fedotov, S. S.; Samarin, A. S.; Antipov, E. V. KTiOPO$_4$-Structured Electrode Materials for Metal-Ion Batteries: A Review. *Journal of Power Sources* **2020**, *480*, 228840. https://doi.org/10.1016/j.jpowsour.2020.228840.

(20) Wernert, R.; Nguyen, L. H. B.; Petit, E.; Camacho, P. S.; Iadecola, A.; Longo, A.; Fauth, F.; Stievano, L.; Monconduit, L.; Carlier, D.; Croguennec, L. Controlling the Cathodic Potential of KVPO4F through Oxygen Substitution. *Chem. Mater.* **2022**, *34* (10), 4523–4535. https://doi.org/10.1021/acs.chemmater.2c00295..

(21) Caracciolo, L.; Madec, L.; Petit, E.; Gabaudan, V.; Carlier, D.; Croguennec, L.; Martinez, H. Electrochemical Redox Processes Involved in Carbon-Coated KVPO$_4$F for High Voltage K-Ion Batteries Revealed by XPS Analysis. *J. Electrochem. Soc.* **2020**, *167* (13), 130527. https://doi.org/10.1149/1945-7111/abbb0c.

(22) Kim, H.; Seo, D.-H.; Bianchini, M.; Clément, R. J.; Kim, H.; Kim, J. C.; Tian, Y.; Shi, T.; Yoon, W.-S.; Ceder, G. A New Strategy for High-Voltage Cathodes for K-Ion Batteries: Stoichiometric KVPO$_4$F. *Adv. Energy Mater.* **2018**, *8* (26), 1801591. https://doi.org/10.1002/aenm.201801591.

(23) Kim, H.; Tian, Y.; Ceder, G. Origin of Capacity Degradation of High-Voltage KVPO$_4$F Cathode. *J. Electrochem. Soc.* **2020**, *167* (11), 110555. https://doi.org/10.1149/1945-7111/aba54e.

(24) Manzi, J.; Brutti, S. Surface Chemistry on LiCoPO4 Electrodes in Lithium Cells: SEI Formation and Self-Discharge. *Electrochimica Acta* **2016**, *222*, 1839–1846. https://doi.org/10.1016/j.electacta.2016.11.175.

(25) Manzi, J.; Vitucci, F. M.; Paolone, A.; Trequattrini, F.; Di Lecce, D.; Panero, S.; Brutti, S. Analysis of the Self-Discharge Process in LiCoPO 4 Electrodes: Bulks. *Electrochimica Acta* **2015**, *179*, 604–610. https://doi.org/10.1016/j.electacta.2015.03.071.

(26) Amine, K.; Yasuda, H.; Yamachi, M. Olivine LiCoPO4 as 4.8 V Electrode Material for Lithium Batteries. *Electrochemical and Solid-State Letters* **2000**, *3* (4), 178–179.

(27) Petříček, V.; Dušek, M.; Palatinus, L. Crystallographic Computing System JANA2006: General Features. *Zeitschrift für Kristallographie - Crystalline Materials* **2014**, *229* (5), 345–352. https://doi.org/10.1515/zkri-2014-1737.

(28) Baur, W. H. The Geometry of Polyhedral Distortions. Predictive Relationships for the Phosphate Group. *Acta Crystallogr B Struct Sci* **1974**, *30* (5), 1195–1215. https://doi.org/10.1107/S0567740874004560.

(29) Bérar, J.-F.; Lelann, P. E.s.d.'s and Estimated Probable Error Obtained in Rietveld Refinements with Local Correlations. *Journal of Applied Crystallography* **1991**, *24* (1), 1–5. https://doi.org/10.1107/S0021889890008391.

(30) Momma, K.; Izumi, F. *VESTA* : A Three-Dimensional Visualization System for Electronic and Structural Analysis. *J Appl Crystallogr* **2008**, *41* (3), 653–658. https://doi.org/10.1107/S0021889808012016.

(31) Ravel, B.; Newville, M. *ATHENA* , *ARTEMIS* , *HEPHAESTUS* : Data Analysis for X-Ray Absorption Spectroscopy Using *IFEFFIT*. *J Synchrotron Rad* **2005**, *12* (4), 537–541. https://doi.org/10.1107/S0909049505012719.

(32) Kresse, G.; Joubert, D. From Ultrasoft Pseudopotentials to the Projector Augmented-Wave Method. *Phys. Rev. B* **1999**, *59* (3), 1758–1775. https://doi.org/10.1103/PhysRevB.59.1758.

(33) Blöchl, P. E. Projector Augmented-Wave Method. *Phys. Rev. B* **1994**, *50* (24), 17953–17979. https://doi.org/10.1103/PhysRevB.50.17953.

(34) Kresse, G.; Hafner, J. *Ab Initio* Molecular Dynamics for Liquid Metals. *Phys. Rev. B* **1993**, *47* (1), 558–561. https://doi.org/10.1103/PhysRevB.47.558.

(35) Kresse, G.; Furthmüller, J. Efficiency of Ab-Initio Total Energy Calculations for Metals and Semiconductors Using a Plane-Wave Basis Set. *Computational Materials Science* **1996**, *6* (1), 15–50. https://doi.org/10.1016/0927-0256(96)00008-0.

(36) Kresse, G.; Hafner, J. *Ab Initio* Molecular-Dynamics Simulation of the Liquid-Metal–Amorphous-Semiconductor Transition in Germanium. *Phys. Rev. B* **1994**, *49* (20), 14251–14269. https://doi.org/10.1103/PhysRevB.49.14251.

(37) Kresse, G.; Furthmüller, J. Efficient Iterative Schemes for *Ab Initio* Total-Energy Calculations Using a Plane-Wave Basis Set. *Phys. Rev. B* **1996**, *54* (16), 11169–11186. https://doi.org/10.1103/PhysRevB.54.11169.

(38) Perdew, J. P.; Burke, K.; Ernzerhof, M. Generalized Gradient Approximation Made Simple. *Phys. Rev. Lett.* **1996**, *77* (18), 3865–3868. https://doi.org/10.1103/PhysRevLett.77.3865.

(39) Dudarev, S. L.; Botton, G. A.; Savrasov, S. Y.; Humphreys, C. J.; Sutton, A. P. Electron-Energy-Loss Spectra and the Structural Stability of Nickel Oxide: An LSDA+U Study. *Phys. Rev. B* **1998**, *57* (3), 1505–1509. https://doi.org/10.1103/PhysRevB.57.1505.

(40) Carlier, D.; Ménétrier, M.; Grey, C. P.; Delmas, C.; Ceder, G. Understanding the NMR Shifts in Paramagnetic Transition Metal Oxides Using Density Functional Theory Calculations. *Phys. Rev. B* **2003**, *67* (17), 174103. https://doi.org/10.1103/PhysRevB.67.174103.

(41) Castets, A.; Carlier, D.; Zhang, Y.; Boucher, F.; Ménétrier, M. A DFT-Based Analysis of the NMR Fermi Contact Shifts in Tavorite-like LiMPO$_4$·OH and MPO$_4$·H$_2$O (M = Fe, Mn, V). *J. Phys. Chem. C* **2012**, *116* (34), 18002–18014. https://doi.org/10.1021/jp302549s.

(42) Castets, A.; Carlier, D.; Zhang, Y.; Boucher, F.; Marx, N.; Croguennec, L.; Ménétrier, M. Multinuclear NMR and DFT Calculations on the LiFePO$_4$·OH and FePO$_4$·H$_2$O Homeotypic Phases. *J. Phys. Chem. C* **2011**, *115* (32), 16234–16241. https://doi.org/10.1021/jp204767c.

(43) Bamine, T.; Boivin, E.; Boucher, F.; Messinger, R. J.; Salager, E.; Deschamps, M.; Masquelier, C.; Croguennec, L.; Ménétrier, M.; Carlier, D. Understanding Local Defects in Li-Ion Battery Electrodes through Combined DFT/NMR Studies: Application to LiVPO$_4$F. *J. Phys. Chem. C* **2017**, *121* (6), 3219–3227. https://doi.org/10.1021/acs.jpcc.6b11747.

(44) Wizansky, R.; Rauch, E.; Disalvo, J. Powerful Oxidizing Agents for the Oxidative Deintercalation of Lithium from Transition-Metal Oxides. *Journal of Solid State Chemistry* **1989**, *81* (2), 203–207. https://doi.org/10.1016/0022-4596(89)90007-8.

TABLE OF CONTENT FIGURE